

Improved Heralded Single-Photon Source with a Photon-Number-Resolving Superconducting Nanowire Detector

Samantha I. Davis^{1,2}, Andrew Mueller,^{2,3} Raju Valivarthi,^{1,2} Nikolai Lauk,^{1,2} Lautaro Narvaez,^{1,2} Boris Korzh,⁴ Andrew D. Beyer^{1,4}, Olmo Cerri^{1,5}, Marco Colangelo^{1,5}, Karl K. Berggren,⁵ Matthew D. Shaw,⁴ Si Xie,^{1,2,6} Neil Sinclair,^{1,2,7} and Maria Spiropulu^{1,2,*}

¹*Division of Physics Mathematics and Astronomy, California Institute of Technology, 1200 E California Boulevard, Pasadena, California 91125, USA*

²*Alliance for Quantum Technologies (AQT), California Institute of Technology, 1200 E California Boulevard, Pasadena, California 91125, USA*

³*Division of Engineering and Applied Science, California Institute of Technology, 1200 E California Boulevard, Pasadena, California 91125, USA*

⁴*Jet Propulsion Laboratory, California Institute of Technology, 4800 Oak Grove Drive, Pasadena, California 91109, USA*

⁵*Department of Electrical Engineering and Computer Science, Massachusetts Institute of Technology, 50 Vassar Street, Cambridge, Massachusetts 02139, USA*

⁶*Fermi National Accelerator Laboratory, P.O. Box 500, Batavia, Illinois 60510, USA*

⁷*John A. Paulson School of Engineering and Applied Sciences, Harvard University, 29 Oxford Street, Cambridge, Massachusetts 02138, USA*



(Received 19 April 2022; revised 22 August 2022; accepted 23 August 2022; published 2 December 2022; corrected 22 December 2022)

Deterministic generation of single photons is essential for many quantum information technologies. A bulk optical nonlinearity emitting a photon pair, where the measurement of one of the photons heralds the presence of the other, is commonly used with the caveat that the single-photon emission rate is constrained due to a trade-off between multiphoton events and pair emission rate. Using an efficient and low noise photon-number-resolving superconducting nanowire detector we herald, in real time, a single photon at telecommunication wavelength. We perform a second-order photon correlation $g^2(0)$ measurement of the signal mode conditioned on the measured photon number of the idler mode for various pump powers and demonstrate an improvement of a heralded single-photon source. We develop an analytical model using a phase-space formalism that encompasses all multiphoton effects and relevant imperfections, such as loss and multiple Schmidt modes. We perform a maximum-likelihood fit to test the agreement of the model to the data and extract the best-fit mean photon number μ of the pair source for each pump power. A maximum reduction of 0.118 ± 0.012 in the photon $g^2(0)$ correlation function at $\mu = 0.327 \pm 0.007$ is obtained, indicating a strong suppression of multiphoton emissions. For a fixed $g^2(0) = 7 \times 10^{-3}$, we increase the single pair generation probability by 25%. Our experiment, built using fiber-coupled and off-the-shelf components, delineates a path to engineering ideal sources of single photons.

DOI: [10.1103/PhysRevApplied.18.064007](https://doi.org/10.1103/PhysRevApplied.18.064007)

I. INTRODUCTION

A challenge in quantum optical science and technology is the realization of an ideal, i.e., deterministic, high-fidelity, tunable, and high-rate, source of indistinguishable single photons [1,2]. One intuitive approach to develop a single-photon source requires coupling an individual quantum emitter to light using a cavity. Significant progress in this regard [3] has been achieved using, e.g., quantum dots [4–6], crystal defects [7], or trapped ions [8]

and atoms [9], albeit mired with challenges, including fabrication complexity [10,11] or differing emitter spectra [12–14]. Instead, the strong light-matter coupling offered by solid-state bulk nonlinearities can be used to probabilistically emit photon pairs via laser-driven $\chi^{(2)}$ and $\chi^{(3)}$ processes [15], i.e., spontaneous parametric down-conversion (SPDC) and four-wave mixing (SFWM), respectively. Thermal statistics of the emission restrict a single-photon pair to be emitted with low probability (e.g., 10^{-3} in practice [16]). An individual photon (in a signal mode) can be heralded by the detection of the other photon (in an idler mode) [1]. Typically this is performed using a threshold detector that discriminates zero from one or more

*Corresponding author. smaria@caltech.edu

photons. Heralding of photons from optical nonlinearities is scalable, and has enabled tunable and indistinguishable photons with high fidelities and bandwidths [1,17,18]. However, there is a nonzero probability to produce multiple pairs. To overcome this obstacle, a photon-number-resolving (PNR) detector at the idler mode can be used to exclude multiphoton events. Notable demonstrations of PNR detection have used, e.g., transition edge sensors and pseudo-PNR detectors constructed from time-multiplexed or arrays of threshold detectors [19–21]. Optimized heralded single-photon sources require scalable, efficient, and low-noise PNR detectors with high timing resolution, that is, low jitter. Here we detect the idler mode from a SPDC process *in real time* using a PNR niobium nitride (NbN) superconducting nanowire single-photon detector (SNSPD) [22]. The detector is optimized across several performance metrics [23]. Specifically, the detection efficiency, which includes coupling loss in the cryostat, is > 0.7 , the dark count rate is 10 Hz, and the jitter is < 14 ps.

To quantify the improvement of our heralded single-photon source, we perform a second-order correlation function $g^2(0)$ measurement [24] of the signal mode conditioned on the measured photon number of the idler mode using the number-resolving detector. This measurement is performed as a function of mean photon-pair number μ of the source.

We operate the detector in two configurations: (i) as a PNR SNSPD, discriminating zero-, one-, and multiphoton events, and (ii) as a threshold SNSPD, discriminating zero-photon events from all other events. A $g^2(0)$ of zero is expected when a single-photon pair is detected. Accounting for loss and multiphoton events, a reduction in $g^2(0)$ is

expected when the detector is operated in configuration (i) versus (ii) for a fixed μ .

Since the measurements extend to large μ , we develop an analytical model for the detection rates, coincidence rates, and $g^2(0)$ using a phase-space formalism that encompasses full multiphoton contributions and all relevant imperfections, such as loss and multiple Schmidt modes [25–27]. We model the PNR detector in phase space as a $2N$ -port beam splitter followed by threshold detection at each output, which allows us to employ Gaussian characteristic function techniques. To evaluate the single-photon discrimination capability of the detector, we define the single-photon discrimination efficiency η_{PNR}^1 metric, ranging from zero, for a threshold detector, to one for an ideal PNR detector. We obtain $\eta_{\text{PNR}}^1 = 0.46$ corresponding to a pseudo-PNR detector comprised of no more than 18 threshold detectors, each with efficiency $\eta_d = 0.71$. We perform a simultaneous maximum-likelihood fit of the model to the measured values of $g^2(0)$ and extract μ for each pump power. We measure a maximum reduction of $g^2(0)$ from 0.430 ± 0.009 to 0.312 ± 0.008 when using configuration (ii) versus (i) at $\mu = 0.327 \pm 0.007$, thereby improving the fidelity of the single-photon source. For a fixed $g^2(0) = 7 \times 10^{-3}$ [28], we increase the probability to generate a single pair by 25%, from 4×10^{-3} to 5×10^{-3} .

II. EXPERIMENTAL METHODS

The experimental setup is shown in Fig. 1. Light pulses of approximately 600-ps duration are created by injecting 1540-nm wavelength light from a continuous-wave laser into an intensity modulator (IM). The modulator is driven by an arbitrary waveform generator (AWG) at a rate

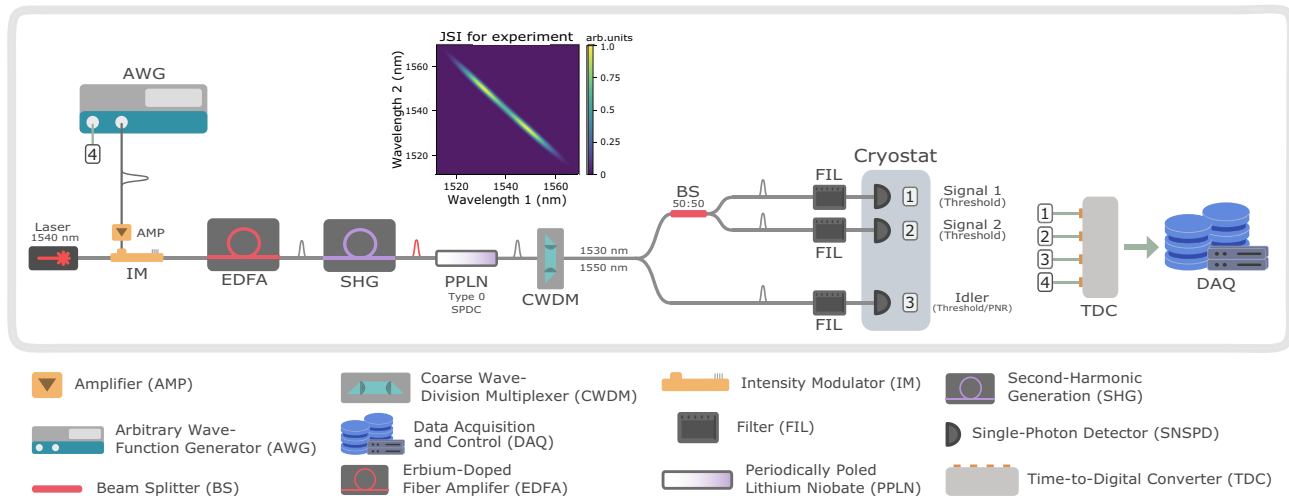


FIG. 1. Experimental setup. AWG, Tektronix AWG7002A; BS, Thorlabs 1550-nm fiber optic 50:50 beam splitter; CWDM, FS one-channel coarse wave-division multiplexing and optical add and drop multiplexer; EDFA, Pritel erbium-doped fiber amplifier; laser, General Photonics TLS-101; PPLN, Covington ruggedized waveguide; SHG, Pritel optical fiber amplifier and second-harmonic generator. The inset shows the estimated joint spectral intensity (JSI) for the experiment including the detector and CWDM response.

$R = 1$ MHz, which is the clock rate of the experiment. The pulses are amplified by an erbium-doped fiber amplifier and then directed to a second-harmonic generation module with a gain-adjusted amplification stage (SHG), which amplifies the pulses then up-converts them to 770-nm wavelength. The pulses are then directed to a fiber-coupled type-0 periodically poled lithium niobate (PPLN) waveguide, which produces photon pairs centered at 1540-nm wavelength via SPDC. A coarse wavelength division multiplexer (CWDM) splits the photon pairs into the signal and idler modes, centered at 1530 and 1550 nm, respectively, each with a 13-nm bandwidth. Light in the signal path is split by a 50:50 beam splitter (BS) into two paths, labeled as signal 1 and 2. Filters with a total of 60-dB extinction on the idler path and 120-dB extinction on the signal path are used to suppress the unconverted 770-nm pump light. The photons from the signal and idler paths are detected using conventional and PNR SNSPDs, respectively.

A. Detectors

The detectors are held at 0.8 K in a Gifford-McMahon cryostat with a ${}^4\text{He}$ sorption stage. To measure the signal modes, we use two single-pixel tungsten silicide (WSi) SNSPDs, which have timing jitters of approximately 50 ps, detection efficiencies of approximately 0.8, and dark count rates below 5 Hz [16]. To measure the idler mode, we use a PNR SNSPD with a timing jitter of < 14 ps, detection efficiency of $\eta_d = 0.71$, and dark counts < 10 Hz. The detector efficiency is determined from an independent measurement similar to that performed in Ref. [29]. The detector has an active area of $22 \times 15 \mu\text{m}^2$, formed by a meander of 100-nm-wide and 5-nm-thick NbN nanowires with a 500-nm pitch. The detector employs a differential architecture to cancel the contribution of the signal propagation delays to the timing jitter [22]. An impedance-matching taper enables photon-number resolution, increases the signal-to-noise ratio, and minimizes reflections as well as distortion [22,30]. The number of incident photons is encoded into the amplitude of the output pulse [22,31]. A single incident photon that is absorbed by the nanowire induces a single time-dependent resistive hotspot, which results in a radio-frequency pulse [23]. Multiple incident photons absorbed by the nanowire at the same time induce multiple time-dependent resistive hotspots. This increases the total resistance of the nanowire, producing a radio-frequency pulse with an amplitude and slew rate that depends on the number of hotspots. In our experiments, rather than measuring the pulse amplitude variation [22,31], we measure its slew-rate variation [32]. This requires only a constant-threshold time tagger, i.e., time-to-digital converter, and enables real-time readout. With a fixed voltage threshold, the variation in slew rate results in a variation of the time of the detection event, i.e., time tag. Earlier (later) time tags, plotted in a histogram in the left (right) bin of Fig. 2,

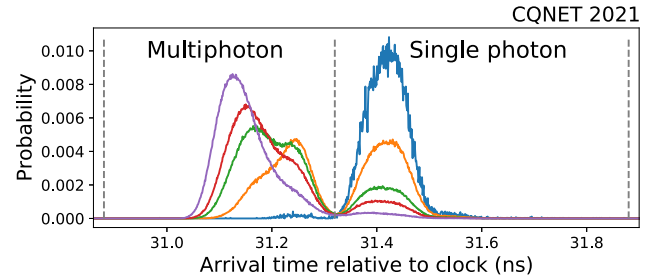


FIG. 2. Probability distribution of the arrival times of detection events by the PNR SNSPD for $\mu \approx 8 \times 10^{-3}$ (blue), $\mu \approx 3$ (orange), $\mu \approx 9$ (green), $\mu \approx 11$ (red), and $\mu \approx 16$ (purple). The dashed lines define the time bins corresponding to single- (right) and multiphoton (left) events. The total number of events in the single- and multiphoton bins are used when operating the SNSPD as a threshold detector, while the number of events in the single-photon bin are used when operating the SNSPD as a PNR detector.

correspond to multiphoton (single-photon) pulses with higher (lower) slew rate.

B. Data acquisition and analysis

The readout pulses from the detectors and the clock signal from the AWG are sent to a time tagger that is interfaced with a custom-made graphical user interface (GUI) for real-time analysis and multiphoton event discrimination. The GUI is depicted in Fig. 3. The recorded detection events in a time bin, that is, the time tags arriving in a temporal interval defined by the red and yellow markers, are collected over a set acquisition time interval. A range of potential arrival times of photons in the signal paths are shown in the top two channels of the

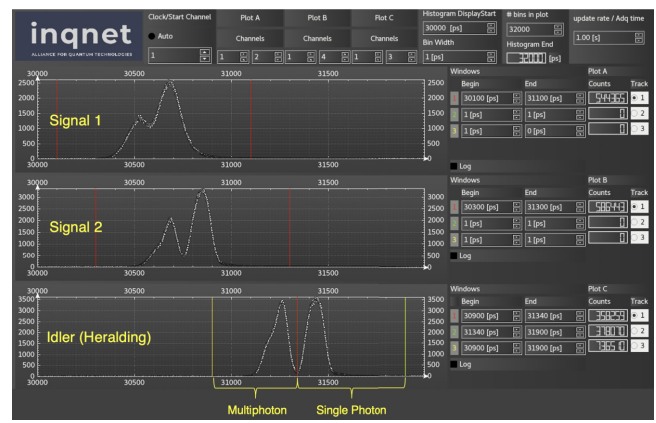


FIG. 3. Custom-made graphical user interface allows time-resolved detection of photons and real-time filtering of multiphoton events. The idler mode depicts a bimodal distribution of time tags relative to the clock for an acquisition time of 1 s. The left bin corresponds to the multiphoton events and the right bin corresponds to the single-photon events.

GUI, and the single and multiphoton events at the idler PNR detector are shown in the bottom channel of the GUI. The GUI is used to collect single-detection events, twofold coincidence events, and threefold coincidence events conditioned on the single- and multiphoton detection events at the idler detector. In other words, the GUI allows collecting all events for analyzing heralding of photons in the signal path conditioned on threshold and PNR detection of photons in the idler path.

C. Characterization

We characterize the setup in two ways: by (1) theoretical calculation and measurement of the joint spectral properties of the photon-pair source and (2) by measuring the signal 1, signal 2, and idler path efficiencies from detection rates with low μ , as described below.

1. Joint spectral intensity

The two photon component of the quantum state describing SPDC at the output of the PPLN waveguide is

$$|\Psi\rangle = A \int_0^\infty \int_0^\infty f(\omega_1, \omega_2) \hat{a}^\dagger(\omega_1) \hat{a}^\dagger(\omega_2) d\omega_1 d\omega_2 |0\rangle,$$

where A is a constant prefactor that depends on the effective nonlinearity and interaction length, $\hat{a}(\omega_1)$ and $\hat{a}(\omega_2)$

are the signal and idler modes with frequencies ω_1 and ω_2 , respectively. The joint spectral amplitude (JSA) is

$$f(\omega_1, \omega_2) = \psi_{\text{ph}}(\omega_1, \omega_2) \cdot \psi_p(\omega_1, \omega_2),$$

comprised of the phase-matching and pump envelope amplitudes $\psi_{\text{ph}}(\omega_1, \omega_2)$ and $\psi_p(\omega_1, \omega_2)$, respectively. The joint spectral intensity (JSI) is $|f(\omega_1, \omega_2)|^2$. We model the phase-matching envelope intensity as

$$|\psi_{\text{ph}}(\omega_1, \omega_2)|^2 = \text{sinc}^2\left(\frac{\Delta k L}{2}\right),$$

where $L = 1$ cm is the length of the waveguide and Δk is the phase mismatch. The calculated phase-matching envelope intensity is depicted in Fig. 4(a). The phase mismatch for co-linear quasi-phase-matching is

$$\Delta k = 2\pi \left(\frac{n(\lambda_p)}{\lambda_p} - \frac{n(\lambda_1)}{\lambda_1} - \frac{n(\lambda_2)}{\lambda_2} - \Gamma \right),$$

where $n_{p(1)(2)}$ is the pump (signal) (idler) index of refraction, $\lambda_{p(1)(2)} = 2\pi c/\omega_{p(1)(2)}$ is the pump (signal) (idler) wavelength, m is an integer, Λ is the poling period of the crystal, and $\Gamma = m/\Lambda = 400 \text{ mm}^{-1}$ [33]. The index of refraction for light of wavelength λ in our PPLN waveguide is approximately

$$n(\lambda) = \sqrt{1 + \frac{2.6734\lambda^2}{\lambda^2 - 0.01764} + \frac{1.2290\lambda^2}{\lambda^2 - 0.05914} + \frac{12.614\lambda^2}{\lambda^2 - 474.60}},$$

where $n(1540 \text{ nm}) = 2.21$ and $n(770 \text{ nm}) = 2.26$ [34]. We model the pump envelope intensity as

$$|\psi_p(\omega_1, \omega_2)|^2 = \exp\left(-\frac{(\omega_p - \omega_1 - \omega_2)^2}{\sigma_p^2}\right),$$

where $\omega_p = 2\pi c/770 \text{ nm}$ and $\sigma_p \sim 2\pi/100 \text{ ps} = 60 \text{ GHz}$, as estimated from independent measurements, which is subject to energy conservation $\omega_p = \omega_1 + \omega_2$. Figure 4(b) shows the calculated pump envelope intensity.

To characterize the photon-pair source, its JSI is determined by performing coincidence measurements of the signal and idler modes after they pass tunable filters with 0.22 nm bandwidths (setup not shown in Fig. 1). The measured JSI accounts for the detector response:

$$|f_m(\omega_1, \omega_2)|^2 = |\psi_{\text{ph}}(\omega_1, \omega_2)|^2 \cdot |\psi_p(\omega_1, \omega_2)|^2 \cdot |\psi_d(\omega_1, \omega_2)|^2, \quad (1)$$

where the third factor is the detector efficiency distribution

$$|\psi_d(\omega_1, \omega_2)|^2 = \exp\left(-\frac{(\lambda_1 - \lambda_d)^2 + (\lambda_2 - \lambda_d)^2}{\sigma_d^2}\right),$$

which we model as a Gaussian centered at the optimal detection wavelength of $\lambda_d = 1550 \text{ nm}$ with a spread of $\sigma_d = 53 \text{ nm}$ found from independently performed detector reflectivity measurements. See Fig. 4(c) for the calculated detector response. The measured JSI including detector response is shown in Fig. 4(d) using circular markers, with brighter color proportional to the rate of coincidence detection events. The contour depicts the theoretical prediction from Eq. (1).

The most relevant JSI is that used for the main experiment, i.e., heralding experiment in configurations (i) with the PNR detector and (ii) with the threshold detector depicted in Fig. 1. This JSI includes the detector response as well as the response of the CWDM. The two output modes of the CWDM are centered at 1550 nm, the idler,

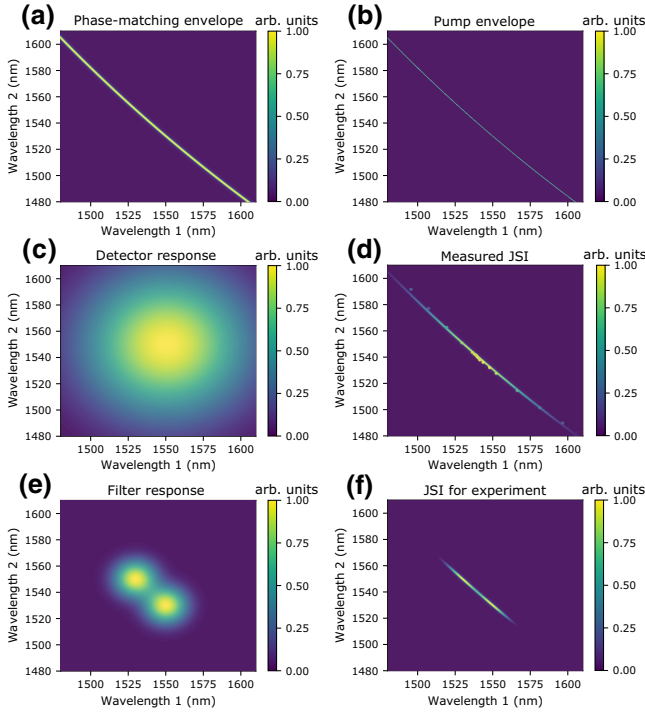


FIG. 4. Measured and theoretically calculated joint spectral information used to characterize the photon-pair source. (a) Phase-matching envelope, (b) pump spectral envelope, (c) detector response, (d) measured (circles) and calculated (contour) JSI, (e) filter response of CWDM, and (f) JSI for the main experiment, also shown in Fig. 1.

and 1530 nm, the signal, with $\sigma_{\text{CWDM}} = 13$ nm bandwidths. Thus, the JSI for the main experiment is modeled as

$$|f_{\text{exp}}(\omega_1, \omega_2)|^2 = |f_m(\omega_1, \omega_2)|^2 \cdot |\psi_f(\omega_1, \omega_2)|^2, \quad (2)$$

with the filter response being

$$|\psi_f(\omega_1, \omega_2)|^2 \approx \exp \left(-\frac{(\lambda_1 - \lambda_{f,1})^2 + (\lambda_2 - \lambda_{f,2})^2}{\sigma_f^2} \right) + \exp \left(-\frac{(\lambda_1 - \lambda_{f,2})^2 + (\lambda_2 - \lambda_{f,1})^2}{\sigma_f^2} \right),$$

where $\lambda_{f,1} = 1550$ nm and $\lambda_{f,2} = 1530$ nm. The theoretical response of the CWDM is shown in Fig. 4(e) whereas Fig. 4(f) depicts the JSI for the main experiment as calculated from Eq. (2).

We perform a Schmidt decomposition of the JSI shown in Fig. 4(f) by calculating the singular value decomposition of Eq. (2) [35]. This is relevant for modeling our $g^2(0)$ results, as discussed in Sec. III, and for determining the fidelity of a heralded single photon, see Sec. V. The obtained eigenvalues λ_s from the decomposition, normalized by their sum over index s , are shown in Fig. 5.

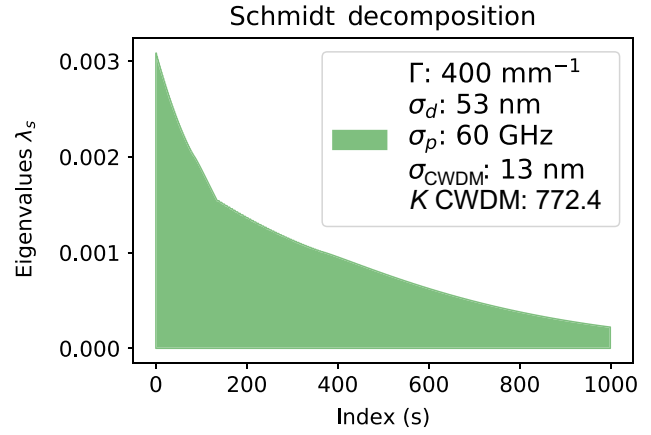


FIG. 5. Eigenvalue spectrum $\sum_s \lambda_s = 1$ obtained from a Schmidt decomposition of the JSI used in the main experiment.

corresponding to a Schmidt number of $K = 1 / \sum_s \lambda_s^2 \approx 772$.

Finally, we determine the sensitivity of the Schmidt decomposition to any potential uncertainty in its key underlying parameters. We independently vary σ_p , σ_{CWDM} , Γ and σ_d , see Eq. (2), and recalculate Schmidt decomposition, with results shown in Fig. 6 and its caption. We find that, unsurprisingly, the variations of the pump σ_p and filter σ_{CWDM} bandwidths have a significant impact on the Schmidt decomposition [36]. Indeed a single spectral mode can be approximated if $\sigma_p >> \sigma_{\text{CWDM}}$ [37]. Consequently, the variations of σ_p and σ_{CWDM} have the largest impact on our theoretical model introduced in Sec. III, and are hence propagated in the fit of the model to the data, see Sec. IV.

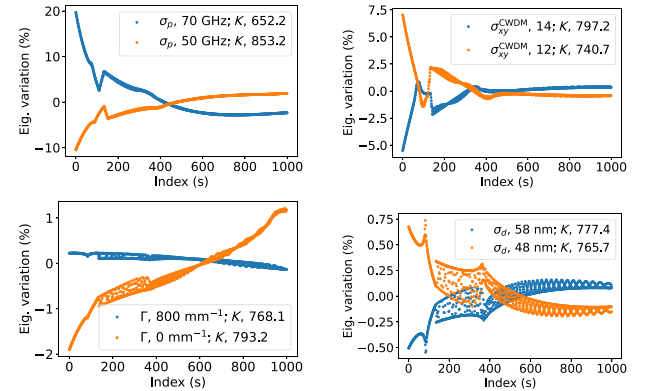


FIG. 6. Sensitivity of the Schmidt eigenvalue decomposition of the JSI for the main experiment is probed by varying key parameters of Eq. (2). Central values and variations for each relevant parameter are as follows: $\sigma_p = 60 \pm 10 \text{ GHz}$, $\sigma_{\text{CWDM}} = 13 \pm 1 \text{ nm}$, $\Gamma = 400 \pm 400 \text{ mm}^{-1}$, and $\sigma_d = 53 \pm 5 \text{ nm}$, with maximum and minimum variations shown. These variations are beyond typical experimental uncertainties and are taken as a worst-case scenario. The variation of each eigenvalue is normalized to the size of the first eigenvalue λ_0 .

2. Path efficiencies

We determine the efficiencies of the signal and idler paths, that is, from PPLN to detection as shown in Fig. 1, by calculating the ratio of coincidence to single-photon detection rates using our photon-pair source [38]. The output of our photon-pair source is a two-mode squeezed vacuum (TMSV) state, and can be approximated as

$$|\psi\rangle_{\text{TMSV}} \approx \sqrt{1-\mu} |0_i 0_s\rangle + \sqrt{\mu} |1_i 1_s\rangle,$$

if $\mu \ll 1$, neglecting loss. In this limit, the probability of generating one pair of photons is given by μ , and can be determined by measuring the coincidence-to-accidental ratio [39]. Correspondingly, the relevant detection rates in our main experiment can be approximated to lowest order in μ :

$$C_i \approx R\eta_i\mu, \quad (3)$$

$$C_{sj} \approx \frac{1}{2}R\eta_{sj}\mu, \quad (4)$$

$$C_{isj} \approx \frac{1}{2}R\eta_i\eta_{sj}\mu, \quad (5)$$

$$C_{s_1 s_2} \approx \frac{1}{2}R\eta_{s_1}\eta_{s_2}\mu^2, \quad (6)$$

$$C_{is_1 s_2} \approx \frac{1}{2}R\mu^2\eta_i\eta_{s_1}\eta_{s_2}(2-\eta_i), \quad (7)$$

where C_i is the detection rate of the idler photons, whereas C_{sj} and C_{isj} are the detection rates of signal j and idler-signal j twofold coincidence events, $j = 1, 2$. The twofold coincidence detection rates for photons in the signal 1 and 2 paths is $C_{s_1 s_2}$ and $C_{is_1 s_2}$ is the rate of threefold coincidence detection events for photons in the idler and the two signal paths. The transmission efficiencies of the idler and two signal paths are η_i and η_{sj} , respectively, and include detector efficiencies.

To estimate the path efficiencies, we calculate the ratios of twofold coincidences to single detection rates the signal 1, signal 2, and idler paths, plotting them in Fig. 7 for varied μ . The amplification in the SHG module is adjusted as a proxy for μ and a linear fit to the data (green line) is used to obtain the average efficiencies and associated uncertainties at $\mu \ll 1$, bounded by the red vertical dashed lines. The mean efficiencies and associated uncertainties (standard deviations) for the signal 1 and 2 paths are $\eta_{s_1} = 2C_{is_1}/C_i = 0.367 \pm 0.009$ and $\eta_{s_2} = 2C_{is_2}/C_i = 0.435 \pm 0.005$, respectively. The idler path efficiency $\eta_i = C_{is_1}/C_{s_1} = 0.319 \pm 0.007$ is estimated from both the PNR and threshold detector configurations. The mean and uncertainty of each path efficiency is used to constraint the fit shown in Fig. 9 of Sec. IV.

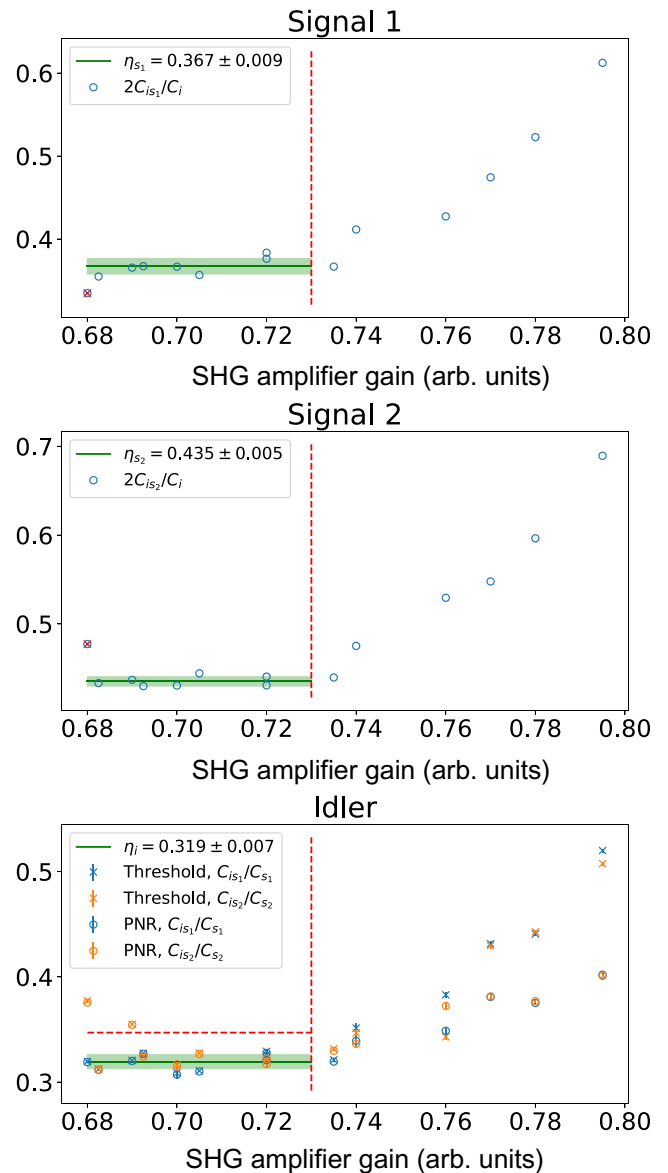


FIG. 7. Ratios of single and twofold coincidence detection rates for the signal and idler paths for varied gain of the amplifier in SHG module. The signal 1, signal 2, and idler path efficiencies, are estimated as shown in the insets using the data on the left (and below) of the red dashed lines, which corresponds to $\mu \ll 1$. Idler efficiencies are measured in configurations with the PNR and threshold detector. The mean and standard deviation of the fitted efficiencies are indicated by green lines, with numerical values in the insets.

III. THEORETICAL MODEL

Photon-pair sources from bulk optical nonlinearities are typically operated at $\mu \ll 1$ to suppress multiphoton events. The $g^2(0)$ measurement performed in our work extends to large μ , where multiphoton contributions are non-negligible and become significantly suppressed in the (i) PNR detection configuration compared to that using

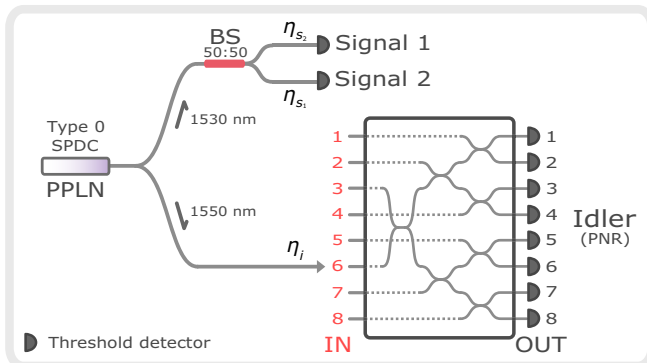


FIG. 8. Schematic of the setup used for theoretical modeling. The PNR detector is modeled as a $2N$ -port beam splitter in a binary tree architecture with threshold detectors at the outputs. Only eight ports are shown in the figure for simplicity. The SPDC source and paths depict a simplified representation of that shown in Fig. 1. The efficiencies, including all coupling and detection loss, of the signal 1, signal 2, and idler paths, are η_{s_1} , η_{s_2} , and η_i , respectively.

(ii) threshold detection. To incorporate full multiphoton effects without approximation, we use methods from the phase-space formulation of quantum optics to derive an expression for $g^2(0)$ as a function of μ . We take into account all major imperfections, including coupling and detector inefficiencies. We note that our model can be extended to include dark counts, which are negligible for our experiment.

A. Characteristic function-based approach

The second-order correlation function of photons in the signal 1 and 2 paths conditioned on the detection of photons in the idler path for both detector configurations (i) and (ii) is

$$g^2(0) = \frac{C_{is_1s_2}C_i}{C_{is_1}C_{is_2}},$$

where $C_{is_1s_2}$ is the rate of threefold coincidence detection events of photons in the idler and signal 1 and 2 paths, C_i is the rate of idler detection events, and C_{is_j} is the twofold coincidence detection rate of idler and signal j events, where $j = 1, 2$. Since we are interested in large μ , we cannot utilize Eqs. (3)–(7). Hence, to find an expression for $g^2(0)$, we derive analytical expressions for the single path detection rates, twofold coincidence rates, and threefold coincidence rates using a characteristic function-based approach [25].

A characteristic function for an N -mode bosonic system is defined as

$$\chi(\xi) = \text{Tr} \left\{ \hat{\rho} \exp(-i(\hat{x}_1, \hat{p}_1, \hat{x}_2, \hat{p}_2, \dots, \hat{x}_N, \hat{p}_N) \cdot \xi) \right\}, \quad (8)$$

where $\hat{\rho}$ is the density matrix describing the state of the system, \hat{x}_i and \hat{p}_i are the conjugate quadrature operators

for mode i , and $\xi \in \mathbb{R}^{2N}$. The quadrature operators can be expressed in terms of the bosonic creation and annihilation operators as

$$\hat{x}_i = \frac{1}{\sqrt{2}} (\hat{a}_i^\dagger + \hat{a}_i), \quad \hat{p}_i = \frac{i}{\sqrt{2}} (\hat{a}_i^\dagger - \hat{a}_i).$$

Equation (8) defines a unique mapping from the space of all possible quantum states to a space of functions over \mathbb{R}^{2N} , i.e., a quantum system is completely characterized by its characteristic function $\chi(\xi)$ [40].

A relevant subclass of quantum states is defined by the states whose characteristic function is given by a multivariate Gaussian function:

$$\chi(\xi) = \exp \left(-\frac{1}{4} \xi^T \gamma \xi - id^T \xi \right),$$

i.e., they are completely characterized by the displacement vector d and covariance matrix γ , corresponding to the first and second moments. Representatives of this subclass include vacuum, coherent, and thermal states as well as single- and two-mode squeezed states.

Relevant for our experiment is the nondegenerate output of a SPDC process, which can be described as a TMSV state whose covariance matrix is given by

$$\begin{aligned} \gamma_{\text{SPDC}}(\mu) &= \begin{pmatrix} \mathbf{A} & \mathbf{B} \\ \mathbf{B} & \mathbf{A} \end{pmatrix}, \\ \mathbf{A} &= \begin{pmatrix} 1+2\mu & 0 \\ 0 & 1+2\mu \end{pmatrix}, \\ \mathbf{B} &= \begin{pmatrix} 2\sqrt{\mu(\mu+1)} & 0 \\ 0 & -2\sqrt{\mu(\mu+1)} \end{pmatrix}, \end{aligned}$$

in block matrix form, where μ is the mean photon-pair number. This description is only valid for a SPDC source where only one signal and one idler mode are present. If the source allows for multiple signal and idler modes, like in the broadband source we use in our experiment, then the initial state must be modified to include all relevant Schmidt modes, determined through the singular value decomposition of the JSI [35], as calculated in Sec. II C 1. In this case, the initial state is a product state of the TMSV states in the corresponding Schmidt modes. The covariance matrix of the system is then given by a direct sum of the covariance matrices of the respective modes

$$\gamma = \gamma_{\text{SPDC}}(\lambda_1\mu) \oplus \gamma_{\text{SPDC}}(\lambda_2\mu) \oplus \dots,$$

for a SPDC source that supports N modes with Schmidt coefficients $\lambda_1, \lambda_2, \dots, \lambda_N$, where the sum runs over all relevant modes, $\lambda_1 \geq \lambda_2 \geq \dots \geq \lambda_N$, and $\sum_{s=1}^N \lambda_s = 1$, as before.

Since linear optics preserves the Gaussian nature of states [40], i.e., it maps Gaussian states onto Gaussian

states, linear optical operations can be described by a symplectic transformation S of the displacement vector and covariance matrix:

$$d' = S^T d, \gamma' = S^T \gamma S.$$

For example, the transformation between the input modes \hat{a} , \hat{b} and the output modes \hat{a}' , \hat{b}' of a beam splitter with transmittivity t is given by

$$\begin{aligned}\hat{a}' &= t\hat{a} + i\sqrt{1-t^2}\hat{b}, \\ \hat{b}' &= t\hat{b} + i\sqrt{1-t^2}\hat{a}.\end{aligned}$$

We can now find the symplectic transformation S of the beam splitter that transforms the quadrature operators:

$$\begin{aligned}\begin{pmatrix} \mathbf{x}_{a'} \\ \mathbf{x}_{b'} \end{pmatrix} &= S^T \begin{pmatrix} \mathbf{x}_a \\ \mathbf{x}_b \end{pmatrix} = \begin{pmatrix} \mathbf{T} & \mathbf{R} \\ \mathbf{R} & \mathbf{T} \end{pmatrix} \begin{pmatrix} \mathbf{x}_a \\ \mathbf{x}_b \end{pmatrix}, \\ \mathbf{x}_i &= (\hat{x}_i, \hat{p}_i)^T, \\ \mathbf{T} &= \begin{pmatrix} t & 0 \\ 0 & t \end{pmatrix}, \quad \mathbf{R} = \begin{pmatrix} 0 & -\sqrt{1-t^2} \\ \sqrt{1-t^2} & 0 \end{pmatrix},\end{aligned}$$

in block matrix form, where $(\mathbf{x}_i, \mathbf{x}_j)^T = (\hat{x}_i, \hat{p}_i, \hat{x}_j, \hat{p}_j)^T$. The beam-splitter transformation is particularly useful because it is used to model path efficiency η_{path} , which is reduced from unity by propagation and coupling loss as well as detector inefficiency. This is accomplished by combining the mode of interest and vacuum on a beam splitter of transmittivity η_{ch} and tracing out the reflected mode.

Given that our setup consists of linear optics, and that loss is modeled as a linear optic transformation, we are able to derive a symplectic transformation S_{system} , with which we calculate the characteristic function of the system up to detection

$$\gamma_{\text{out}} = S_{\text{system}}^T \gamma_{\text{in}} S_{\text{system}}.$$

From the covariance matrix of the final Gaussian state, we can calculate several relevant experimental values such as detection probabilities or rates, which can be used to predict key figures of merit, such as fringe visibilities or state fidelities of qubits [16].

Concerning the photon detection step, consider a measurement operator $\hat{\Pi}$. The probability of detecting the measurement outcome for a given state $\hat{\rho}$ is

$$\text{Tr}[\hat{\rho} \hat{\Pi}] = \left(\frac{1}{2\pi}\right)^N \int dx^{2N} \chi_\rho(x) \chi_\Pi(-x), \quad (9)$$

where $\chi_\Pi(-x)$ is the characteristic function of the measurement operator and is defined in the same way as Eq. (8) but with $\hat{\Pi}$ instead of $\hat{\rho}$. For threshold detectors, which destructively discriminate between nonzero

and zero photons, that is, a detection event and nonevent, their measurement operators are

$$\begin{aligned}\hat{\Pi}_{\text{no event}} &= |0\rangle \langle 0|, \\ \hat{\Pi}_{\text{event}} &= \hat{I} - |0\rangle \langle 0|,\end{aligned}$$

i.e., we can model the threshold detectors by projections onto the vacuum state. Since the vacuum state is a Gaussian state, the integrand in Eq. (9) is a multivariate Gaussian function yielding

$$\text{Tr}[\hat{\rho} \hat{\Pi}_{\text{no event}}] = \frac{2^{N_{\text{meas}}}}{\sqrt{\det(\gamma_{\text{red}} + I_{\text{red}})}} e^{-d_{\text{red}}^T (\gamma_{\text{red}} + I_{\text{red}})^{-1} d_{\text{red}}}, \quad (10)$$

where N_{meas} is the number of modes being measured, γ_{red} is the reduced covariance matrix, and d_{red} is the reduced displacement vector obtained from γ and d by tracing out all modes but those measured.

B. Photon-number-resolving detector

Since the measurement operators describing PNR detectors are not Gaussian operators [41], we cannot evaluate Eq. (10) to find the probability of detecting one or more photons for the PNR detector. Instead, we model the PNR detector as an effective $2N$ -port beam splitter with threshold detectors at each output port [21,26,27,42]. We implement the $2N$ -port beam splitter as a network of beam splitters forming a so-called “binary tree” architecture, which has N input and output ports, as depicted in Fig. 8 for the case $N = 8$.

To model a PNR detector, photons are injected to an input of the “top-most” beam splitter of the tree, e.g., input 6 in Fig. 8. The detection of photons with the PNR SNSPD is modeled as detection events from any combination of threshold detectors at the output ports of the tree. For an input Fock state $|n\rangle$, the probability that multiple photons arrive to the same output port is negligible when $N \gg n$, corresponding to ideal photon-number discrimination. In this case, the number of detection events equals the number of input photons. For $N \sim n$, the probability of multiple photons arriving to the same output port is non-negligible, corresponding to nonideal photon-number discrimination. In this case, the number of detection events does not equal the number of input photons. Therefore, the depth of the tree $k = \log_2(N)$, is a figure of merit for photon-number discrimination.

With our beam-splitter tree and threshold detector model, we are able to employ Gaussian characteristic function techniques to find photon detection probabilities, which we later employ to calculate coincidence detection probabilities, and hence detection rates. We append $N - 1$ vacuum modes to the state at idler mode and find the symplectic matrix that transforms the characteristic function of

the input state to the tree to that of the output state. The symplectic matrix S_k of a beam-splitter tree with depth k can be constructed using the recursive symmetry of the binary tree architecture

$$S_k = (S_{k-1} \oplus S_{k-1})S_{k,t},$$

where $S_{k,t}$ is the symplectic matrix corresponding to the top-most beam splitter for a tree with depth k . The covariance matrix γ_N and displacement vector d_N of the N -mode input state to the tree then transform as

$$d'_N = S_k^T d_N, \gamma'_N = S_k^T \gamma_N S_k,$$

which is followed by threshold detection at each of the N outputs.

The probability of detecting nonzero photons at m of the modes, i.e., having a m -fold coincidence event, for an N -mode Gaussian state with covariance matrix γ_N is

$$\begin{aligned} & \sum_{\{m\}} \text{Tr}[\hat{\rho}^{\gamma_N} (\hat{\Pi}_{\text{event}}^{\otimes m} \otimes \hat{\Pi}_{\text{no-event}}^{\otimes(N-m)})] \\ &= \sum_{\{m\}} \text{Tr}[\hat{\rho}^{\gamma_N} ((\hat{I} - |0\rangle\langle 0|)^{\otimes m} \otimes |0\rangle\langle 0|^{\otimes(N-m)})], \end{aligned}$$

where $\sum_{\{m\}}$ indicates a sum over the all possible choices of m output modes. This results in a linear combination of $\binom{N}{m}$ terms of the form

$$\text{Tr}[\hat{\rho}^{\gamma_N} (\hat{I}^{\otimes j} \otimes |0\rangle\langle 0|^{\otimes(N-j)})] = \text{Tr}[\hat{\rho}_{\text{red}}^{\gamma_N} |0\rangle\langle 0|^{\otimes(N-j)}], \quad (11)$$

where $\hat{\rho}_{\text{red}}^{\gamma_N}$ is the reduced density matrix of the system obtained by taking a partial trace over j modes with $0 \leq j \leq N$. One useful property of Gaussian states is that the covariance matrix of the reduced state after a partial trace is simply the submatrix corresponding to the remaining system. It can be shown that for an N -mode system with covariance matrix γ_N and displacement vector d_N , the probability of measuring zero photons across the N modes is

$$\begin{aligned} \text{Tr}[\hat{\rho} \hat{\Pi}_{\text{no event}}^{\otimes N}] &= \text{Tr}[\hat{\rho} |0\rangle\langle 0|^{\otimes N}] \\ &= \frac{2^N}{\sqrt{\det(\gamma_N + I_N)}} e^{-d_N^T (\gamma_N + I_N)^{-1} d_N}. \end{aligned}$$

Equation (11) then simplifies to

$$\begin{aligned} \text{Tr}[\hat{\rho}_{\text{red}}^{\gamma_N} |0\rangle\langle 0|^{\otimes(N-j)}] &= \frac{2^{N-j}}{\sqrt{\det(\gamma_{N-j} + I_{N-j})}} e^{-d_{N-j}^T (\gamma_{N-j} + I_{N-j})^{-1} d_{N-j}}, \end{aligned}$$

where I_m is the m by m identity matrix, γ_{N-j} is the submatrix of γ_N , and d_{N-j} is the subvector of d_N corresponding

to the remaining subsystem of $N - j$ modes. By knowing γ_N and d_N of the full N -mode system, we can find the m -fold coincidence event probability for arbitrary m , where $0 \leq m \leq N$.

For our experiment, we are interested in the single-photon detection probability P_1^N of the PNR detector. We model this as the probability that a single output mode of the beam-splitter tree contains a photonic excitation:

$$\begin{aligned} P_1^N &= N \text{Tr}[\hat{\rho}^{\gamma'_N} (\hat{\Pi}_{\text{event}} \otimes \hat{\Pi}_{\text{no event}}^{\otimes(N-1)})] \\ &= \frac{N 2^{N-1}}{\sqrt{\det(\gamma'_{N-1} + I_{N-1})}} e^{-d'_{N-1}^T (\gamma'_{N-1} + I_{N-1})^{-1} d'_{N-1}} \\ &\quad - \frac{N 2^N}{\sqrt{\det(\gamma'_N + I_N)}} e^{-d_N^T (\gamma'_N + I_N)^{-1} d'_N}. \end{aligned} \quad (12)$$

We can also use the $2N$ -port beam-splitter model to describe the photon-number discrimination capability of the detector, as discussed in the following sections.

1. Photon-number detection

When a single photon is sent to an input of the $2N$ -port beam splitter, the action of the beam splitter corresponding to unitary U_N splits the photon into an equal superposition of the N output modes. An arbitrary Fock state $|n\rangle$ directed to a single input port transforms as

$$U_N |n\rangle = \frac{1}{(\sqrt{N})^n} \sum_{j_1+\dots+j_N=n} \sqrt{\frac{n!}{j_1! \cdots j_N!}} |j_1\rangle \cdots |j_N\rangle,$$

Thus, the joint probability of finding j_1 photons at output 1, j_2 photons at output 2, ..., and j_N photons at output N is

$$P_n(j_1, \dots, j_N) = \frac{1}{N^n} \frac{n!}{j_1! \cdots j_N!}, \text{ where } \sum_{i=1}^N j_i = n.$$

The probability that n photons at a single input port trigger an m -fold coincidence event, i.e., a detection at each of the m output ports, is

$$P_{m,n}^N = \frac{n!}{N^n} \sum_{j_1+\dots+j_N=n}^{(m)} \frac{1}{j_1! \cdots j_N!} = \frac{m!}{N^n} \binom{N}{m} S_2(n, m), \quad (13)$$

where $1 \leq m \leq n$, the notation (m) refers to the condition that m of $\{j_i\}$ are nonzero, and $S_2(n, m)$ is the Stirling number of the second kind. The Stirling number corresponds to the number of ways of partitioning a set of n elements into m nonempty sets [43].

As $N \rightarrow \infty$, the $2N$ -port model approaches a PNR detector with perfect discrimination efficiency, such that the single-photon detection probability equals the single-photon probability of a general input state,

$$\lim_{N \rightarrow \infty} P_1^N = \langle 1 | \rho^{\gamma_N'} | 1 \rangle.$$

For example, from Eq. (12), we can find the probability of a detection event at one output of a tree with depth k for an input thermal state with mean photon number μ as

$$P_1^k = \frac{2^k \mu}{(1 + \mu)(2^k + (2^k - 1)\mu)}.$$

Similarly, for a coherent state with mean photon number $|\alpha|^2$ as

$$P(1)_k = 2^k e^{-|\alpha|^2} \left(e^{|\alpha|^2/2^k} - 1 \right).$$

By taking the limit $k \rightarrow \infty$, we recover the single-photon probabilities for a thermal state and coherent state, respectively, as

$$\begin{aligned} \lim_{k \rightarrow \infty} \frac{2^k \mu}{(1 + \mu)(2^k + (2^k - 1)\mu)} &= \frac{\mu}{(1 + \mu)^2}, \\ \lim_{k \rightarrow \infty} 2^k e^{-|\alpha|^2} \left(e^{|\alpha|^2/2^k} - 1 \right) &= e^{-|\alpha|^2} |\alpha|^2. \end{aligned}$$

2. POVM elements and counting statistics

The values of $P_{m,n}^N$, from Eq. (13), correspond to the matrix elements of a conditional probability matrix \mathbf{C} , following the definition used in Ref. [27]. The rows correspond to the positive operator-value measure (POVM) elements of the measurement outcomes and the columns correspond to the Fock projection operators. The matrix for a threshold detector, in other words, a tree with $k = 0$ is

$$\hat{\Pi}_{\text{no event}} \quad \left(\begin{array}{ccccccccc} |0\rangle \langle 0| & |1\rangle \langle 1| & |2\rangle \langle 2| & |3\rangle \langle 3| & |4\rangle \langle 4| & |5\rangle \langle 5| & |6\rangle \langle 6| & \cdots \\ 1 & 0 & 0 & 0 & 0 & 0 & 0 & \cdots \\ 0 & 1 & 1 & 1 & 1 & 1 & 1 & \cdots \end{array} \right),$$

with measurement outcomes (rows) and projections (columns) indicated. The matrix for an ideal PNR detector is the identity matrix

$$\hat{\Pi}_0 \quad \left(\begin{array}{ccccccccc} |0\rangle \langle 0| & |1\rangle \langle 1| & |2\rangle \langle 2| & |3\rangle \langle 3| & |4\rangle \langle 4| & |5\rangle \langle 5| & |6\rangle \langle 6| & \cdots \\ 1 & 0 & 0 & 0 & 0 & 0 & 0 & \cdots \\ 0 & 1 & 0 & 0 & 0 & 0 & 0 & \cdots \\ 0 & 0 & 1 & 0 & 0 & 0 & 0 & \cdots \\ 0 & 0 & 0 & 1 & 0 & 0 & 0 & \cdots \\ 0 & 0 & 0 & 0 & 1 & 0 & 0 & \cdots \\ 0 & 0 & 0 & 0 & 0 & 1 & 0 & \cdots \\ 0 & 0 & 0 & 0 & 0 & 0 & 1 & \cdots \\ \vdots & \ddots \end{array} \right).$$

For a detector with efficiency η_d , i.e., modeled as path loss of transmittivity η_d before an ideal detector, the probability that n photons trigger an m -fold coincidence detection event is

$$\begin{aligned} P_{m,n}^N(\eta_d) &= \sum_{j=0}^n P_{m,j}^N \binom{n}{j} \eta_d^j (1 - \eta_d)^{n-j} \\ &= \sum_{j=0}^n C_{m,j} L_{j,n} \\ &= (\mathbf{C} \cdot \mathbf{L})_{m,n}, \end{aligned}$$

where \mathbf{L} is the loss matrix with matrix elements,

$$L_{j,n} = \binom{n}{j} \eta_d^j (1 - \eta_d)^{n-j}.$$

The matrix corresponding to $\mathbf{C} \cdot \mathbf{L}$ for a tree with $k = 3$ and $\eta_d = 0.71$ is

$$\hat{\Pi}_0 \quad \begin{pmatrix} |0\rangle\langle 0| & |1\rangle\langle 1| & |2\rangle\langle 2| & |3\rangle\langle 3| & |4\rangle\langle 4| & |5\rangle\langle 5| & |6\rangle\langle 6| & \dots \\ 1 & 0.29 & 0.084 & 0.024 & 0.007 & 0.002 & 0.001 & \dots \\ 0 & 0.71 & 0.475 & 0.240 & 0.108 & 0.046 & 0.019 & \dots \\ 0 & 0 & 0.441 & 0.501 & 0.383 & 0.246 & 0.144 & \dots \\ 0 & 0 & 0 & 0.235 & 0.398 & 0.425 & 0.368 & \dots \\ 0 & 0 & 0 & 0 & 0.104 & 0.244 & 0.346 & \dots \\ 0 & 0 & 0 & 0 & 0 & 0.037 & 0.114 & \dots \\ 0 & 0 & 0 & 0 & 0 & 0 & 0.010 & \dots \\ \vdots & \ddots \end{pmatrix}$$

As we show in detail in Sec. IV, this matrix corresponds to our experimental PNR configuration.

The counting statistics $p(n)$ can be related to the input photon-number distribution $\varrho(n)$ by

$$p_m = \sum_n \sum_{j=0}^n C_{m,j} L_{j,n} \varrho_n,$$

where $p_m = p(m)$ and $\varrho_n = \varrho(n)$, following the notation of Eq. (9) from Ref. [27]. In matrix notation this is $\vec{p} = \mathbf{C} \cdot \vec{\varrho}$. The transpose of the matrix $(\mathbf{C} \cdot \mathbf{L})^T$ is matrix \mathbf{B} from Ref. [26], which relates probabilities and density matrices as $\vec{p} = \mathbf{B}\hat{\rho}$.

3. Photon-number discrimination efficiency

A key figure of merit of our detector PNR configuration is its ability to discriminate single-photon events from others. To quantify this, we define the “ m -photon discrimination efficiency” and use it to calculate the “single-photon discrimination efficiency” as follows.

A POVM element corresponding to the m -photon outcome for a nonideal PNR detector can be described by

$$\hat{\Pi}_m = \sum_{n=0}^{\infty} c_n^m |n\rangle\langle n|, \quad (14)$$

where c_n^m are the matrix elements corresponding to the representation of the operator in the photon-number basis, and are each equal to the probability of registering m photons given n incident photons. The m -photon outcome for an ideal PNR detector is

$$\hat{\Pi}_m^{\text{ideal}} = |m\rangle\langle m|. \quad (15)$$

Note that for a threshold detector, the m -photon outcome for $m > 0$ is the “event” outcome $\hat{\Pi}_{\text{event}} = \sum_{n=1}^{\infty} |n\rangle\langle n|$,

and $m = 0$ outcome corresponds to “no event” $\hat{\Pi}_{\text{no event}} = |0\rangle\langle 0|$. We define the m -photon discrimination efficiency as

$$\eta_{\text{PNR}}^m = 1 - \frac{1}{2} \text{Tr} \left[\sqrt{\left(\frac{\hat{\Pi}_m}{\text{Tr}[\hat{\Pi}_m]} - \frac{\hat{\Pi}_m^{\text{ideal}}}{\text{Tr}[\hat{\Pi}_m^{\text{ideal}}]} \right)^2} \right], \quad (16)$$

where the second term is the trace distance between elements $\hat{\Pi}_m$ and $\hat{\Pi}_m^{\text{ideal}}$, normalized by their trace, corresponding to the m -photon measurement outcome of the PNR detector. Using Eqs. (14) and (15), we simplify Eq. (16) to

$$\eta_{\text{PNR}}^m = \frac{c_m^m}{\sum_{n=0}^{\infty} c_n^m} = \frac{P(m|m)}{\sum_{n=0}^{\infty} P(m|n)}, \quad (17)$$

where $c_n^m = P(m|n)$ is the probability that the detector registers m photons given that n photons were incident on the detector. Relevant to our experiment is the single-photon discrimination efficiency ($m = 1$). As defined in Eq. (17), η_{PNR}^1 is zero for a threshold detector and unity for an ideal PNR detector.

C. Analytical expressions of detection probabilities

For a $2N$ -port beam splitter realized as a finite-depth binary tree, we derive the following expressions for detection probabilities of the signal and idler paths, as well as twofold and threefold coincidence event probabilities as a function of the efficiencies and tree depth k , where $N = 2^k$. The equations reduce to the threshold detection case for $k = 0$.

We use $\hat{\Pi}_{\text{no event},m}$ and $\hat{\Pi}_{\text{event},m}$ to denote the measurement operators for a threshold detector at the m th tree output:

$$\begin{aligned}\hat{\Pi}_{\text{no event},m} &= |0\rangle \langle 0|_m, \\ \hat{\Pi}_{\text{event},m} &= \hat{I}_m - |0\rangle \langle 0|_m.\end{aligned}$$

For the PNR detector, we use $\hat{\Pi}_{\text{event},m} \otimes \hat{\Pi}_{\text{no event}}^{\otimes N-1}$ to denote an “event” measurement outcome for a detector at the m th output and “no event” measurement outcomes for the detectors at the remaining $N-1$ outputs of the tree.

1. Detection probabilities for signal and idler detectors

The probabilities P_{s_1} and P_{s_2} of a detection event for the signal 1 and 2 detectors, respectively, are

$$\begin{aligned}P_{s_1} &= \text{Tr} \left[\rho \left(\hat{\Pi}_{s_1, \text{event}} \otimes \hat{I}_{s_2} \otimes \hat{I}^{\otimes N} \right) \right], \\ P_{s_2} &= \text{Tr} \left[\rho \left(\hat{I}_{s_1} \otimes \hat{\Pi}_{s_2, \text{event}} \otimes \hat{I}^{\otimes N} \right) \right],\end{aligned}$$

and evaluate to

$$P_{s_j} = 1 - \prod_s \frac{2}{2 + \eta_{s_j} \lambda_s \mu},$$

where $j = 1, 2$, and λ_s are the Schmidt coefficients obtained from the singular value decomposition of the JSI as discussed in Sec. II C 1. The products in the expressions run over all Schmidt coefficients. The mean number of pairs μ as well as path efficiencies η_i and η_{s_j} , where

$j = 1, 2$, as depicted in Fig. 8 and used here and in the following, are as defined earlier.

The probability P_i of a detection event for the idler detector is then

$$P_i = N \text{Tr} \left[\rho \left(I_{s_1} \otimes I_{s_2} \otimes \hat{\Pi}_{\text{event},m} \otimes \hat{\Pi}_{\text{no event}}^{\otimes N-1} \right) \right],$$

and evaluates to

$$P_i = 2^k \left(\prod_s \frac{2^k}{2^k + (2^k - 1)\lambda_s \mu \eta_i} - \prod_s \frac{1}{1 + \lambda_s \mu \eta_i} \right). \quad (18)$$

2. Twofold coincidence detection probabilities

The probabilities of a twofold coincidence detection event at the idler and one of the signal detectors, P_{is_1} and P_{is_2} , are

$$\begin{aligned}P_{is_1} &= N \text{Tr} \left[\rho \left(\hat{\Pi}_{\text{event},s_1} \otimes I_{s_2} \otimes \hat{\Pi}_{\text{event},m} \otimes \hat{\Pi}_{\text{no event}}^{\otimes N-1} \right) \right], \\ P_{is_2} &= N \text{Tr} \left[\rho \left(I_{s_1} \otimes \hat{\Pi}_{\text{event},s_2} \otimes \hat{\Pi}_{\text{event},m} \otimes \hat{\Pi}_{\text{no event}}^{\otimes N-1} \right) \right],\end{aligned}$$

and evaluate to

$$\begin{aligned}P_{is_j} &= 2^k \left(\prod_s \frac{2^k}{2^k + (2^k - 1)\lambda_s \mu \eta_i} - \prod_s \frac{2^{k+1}}{\lambda_s \mu \eta_{s_j} (2^k - (2^k - 1)\eta_i) + 2(2^k + (2^k - 1)\lambda_s \mu \eta_i)} \right. \\ &\quad \left. - \prod_s \frac{1}{1 + \lambda_s \mu \eta_i} + \prod_s \frac{2}{2 + 2\lambda_s \mu \eta_i + \eta_{s_j} \lambda_s \mu (1 - \eta_i)} \right), \quad (19)\end{aligned}$$

where $j = 1, 2$.

The probability of a twofold coincidence detection event at the signal 1 and 2 detectors is

$$P_{s_1 s_2} = \text{Tr} \left[\rho \left(\hat{\Pi}_{\text{event},s_1} \otimes \hat{\Pi}_{\text{event},s_2} \otimes \hat{I}_m^{\otimes N} \right) \right],$$

and evaluates to

$$\begin{aligned}P_{s_1 s_2} &= 1 - \prod_s \frac{2}{2 + \eta_{s_1} \lambda_s \mu} - \prod_s \frac{2}{2 + \eta_{s_2} \lambda_s \mu} \\ &\quad + \prod_s \frac{2}{2 + (\eta_{s_1} + \eta_{s_2}) \lambda_s \mu}.\end{aligned}$$

3. Threefold coincidence detection probabilities

The probability of a threefold coincidence detection event at the idler, signal 1, and signal 2 detectors, $P_{i,s_1,s_2}(\mu, \eta_{s_1}, \eta_{s_2}, \eta_i, k)$, is

$$P_{i,s_1,s_2} = N \text{Tr} \left[\rho \left(\hat{\Pi}_{\text{event},s_1} \otimes \hat{\Pi}_{\text{event},s_1} \otimes \hat{\Pi}_{\text{event},m} \otimes \hat{\Pi}_{\text{no event}}^{\otimes N-1} \right) \right],$$

and evaluates to

$$\begin{aligned} P_{i,s_1,s_2} = & 2^k \left(\prod_s \frac{2^k}{(2^k + (2^k - 1)\lambda_s \mu \eta_i)} - \prod_s \frac{2^{k+1}}{\lambda_s \mu \eta_{s_1} (2^k - (2^k - 1)\eta_i) + 2(2^k + (2^k - 1)\lambda_s \mu \eta_i)} \right. \\ & - \prod_s \frac{2^{k+1}}{\lambda_s \mu \eta_{s_2} (2^k - (2^k - 1)\eta_i) + 2(2^k + (2^k - 1)\lambda_s \mu \eta_i)} \\ & + \prod_s \frac{2^{k+1}}{\lambda_s \mu (\eta_{s_1} + \eta_{s_2}) (2^k - (2^k - 1)\eta_i) + 2(2^k + (2^k - 1)\lambda_s \mu \eta_i)} \\ & - \prod_s \frac{1}{1 + \lambda_s \mu \eta_i} + \prod_s \frac{2}{2 + 2\lambda_s \mu \eta_i + \eta_{s_1} \lambda_s \mu (1 - \eta_i)} + \prod_s \frac{2}{2 + 2\lambda_s \mu \eta_i + \eta_{s_2} \lambda_s \mu (1 - \eta_i)} \\ & \left. - \prod_s \frac{2}{2 + 2\mu \lambda_s \eta_i + (\eta_{s_1} + \eta_{s_2}) \mu \lambda_s (1 - \eta_i)} \right). \end{aligned} \quad (20)$$

4. Second-order correlation function $g^{(2)}(0)$

Finally, we readily derive the analytical expression for $g^{(2)}(0)$ by substituting Eqs. (18), (19), and (20) into

$$g^{(2)}(0) = \frac{P_{i,s_1,s_2} P_i}{P_{i,s_1} P_{i,s_2}} = \frac{C_{i,s_1,s_2} C_i}{C_{i,s_1} C_{i,s_2}}, \quad (21)$$

where the respective probabilities P can be used to calculate detection rates C using $C = RP$.

IV. RESULTS

We vary the gain of the amplifier in the SHG module and measure single detector, i.e., signal 1 and 2 and idler, events as well as two- and threefold coincidence detection events for (i) the PNR configuration and (ii) the threshold configuration for the idler detector. We then perform a maximum-likelihood fit of our theoretical model for $g^{(2)}(0)$, i.e., Eq. (21), to the measured $g^{(2)}(0)$ for configurations (i) with PNR and (ii) with threshold detection. The likelihood is optimized using the MINUIT [44] implementation in *iminuit* [45]. The experimental $g^{(2)}(0)$ data and curve corresponding to the best-fitted model are shown in Fig. 9.

A. Maximum-likelihood fit

The theoretical model for $g^{(2)}(0)$ includes several parameters, as introduced in Secs. II and III. Our fit extracts the following key experimental values: mean photon-pair number μ , tree depth k , path efficiencies η_i , η_{s_1} , and η_{s_2} ,

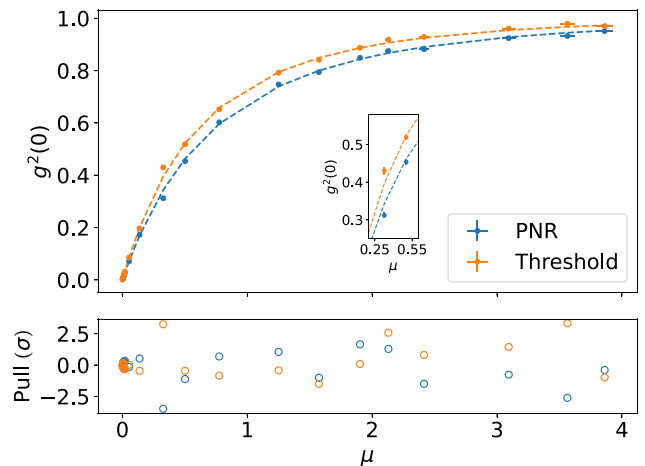


FIG. 9. Measured correlation function $g^{(2)}(0)$ as a function of mean photon-pair number μ . The experimental data using threshold (orange) and PNR (blue) idler detector configurations are represented by the circular markers whereas the respective fitted models are shown by dashed lines. Uncertainties of $g^{(2)}(0)$, referred to as $\sigma_{g^{(2)}(0)}$, are derived from the statistical uncertainties of the coincidence detection events whereas the uncertainties of μ , that is, σ_μ , are extracted from the fit to the model. The inset depicts the region where the largest reduction in $g^{(2)}(0)$ is measured. The pull between the measured $g^{(2)}(0)$ and the model, computed as $[\sigma_{g^{(2)}(0)}^2 + |\partial_\mu g^{(2)}(0)|^2 \sigma_\mu^2]^{1/2}$ and plotted in units of standard deviations, is shown at the bottom of the canvas.

TABLE I. Maximum-likelihood best-fit results for key experimental parameters. Uncertainties are computed by inverting the Hessian, except for k , where a likelihood scan has been performed. There is no value of pull for k as it is extracted from a fit without a constraint.

Parameter	Best fit	Pull (σ)
η_i	0.319 ± 0.026	$-0.1 (3.9)$
η_{s1}	0.370 ± 0.024	$0.3 (2.5)$
η_{s2}	0.436 ± 0.017	$0.2 (3.3)$
σ_{CWDM} (nm)	11.97 ± 0.95	$-1.0 (0.9)$
σ_p (GHz)	87.7 ± 14.0	$2.8 (1.4)$
k	$3.45^{+0.71}_{-0.50}$	

as well as the filter and pump bandwidths, σ_{CWDM} and σ_p , which strongly influence the eigenvalue spectrum of JSI. The best-fit values and uncertainties of the mean photon number for each amplifier setting is shown in Fig. 9. We also calculate the pull for $g^2(0)$, which is the distance of the best-fit value from the Gaussian constraint measured in values of the constraint width. The best fit, uncertainties, and pull of the other values are shown in Table I. We find the best-fit path efficiencies and the filter bandwidth are identical, within uncertainty, to that evaluated by independent measurements in Secs. II C 2 and II C 1. The predicted pump bandwidth (88 GHz) is larger than that measured

in Sec. II C 1 (60 GHz) likely because it was inferred by measurements at telecommunication wavelength.

In the fit, the path efficiencies are free parameters, while the mean and uncertainties thereof, measured in Sec. II C 2, are used to place Gaussian constraints on the fit. Each measured $g^2(0)$ is ascribed an independent value of μ , and given the path efficiencies, is determined by fitting the single detector and twofold coincidence detection probabilities, i.e., those shown in Fig. 10, collected during the measurements. The mean and statistical uncertainties of these detection rates is used to place a Gaussian constraint on the value of μ for each data point. The eigenvalue spectrum of the JSI is computed by varying $\sigma_{\text{CWDM}} = 13 \pm 1$ nm and $\sigma_p = 60 \pm 10$ GHz as discussed in Sec. II C 1, and a linear approximation is used to allow the fit for a continuous variation. Additional fit details are discussed in the captions of Fig. 9 and Table I.

B. Single-photon discrimination efficiency

With $k = 3.45^{+0.71}_{-0.50}$ extracted from the fit, the single-photon discrimination efficiency of our PNR detector is comparable to that of a pseudo-PNR detector comprised of approximately 11^{+7}_{-3} threshold detectors, each with efficiency $\eta_d = 0.71$. Therefore, following the model developed in Sec. III B 2, the experimental POVM is

$$\hat{\Pi}_1^{\text{exp}} \approx 0.710 |1\rangle \langle 1| + 0.458 |2\rangle \langle 2| + 0.222 |3\rangle \langle 3| + 0.096 |4\rangle \langle 4| + 0.039 |5\rangle \langle 5| + 0.015 |6\rangle \langle 6|, \quad (22)$$

corresponding, according to the arguments in Sec. III B 3, to a single-photon discrimination efficiency of $\eta_{\text{PNR}}^1 \approx 0.46$, limited mainly by η_d .

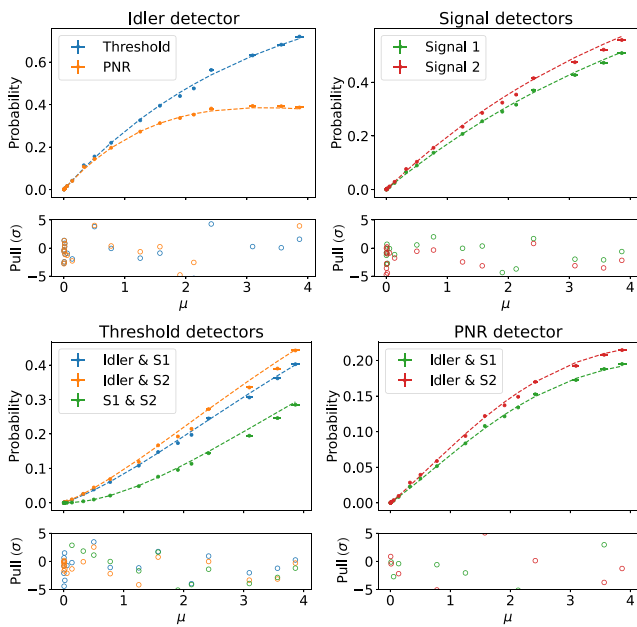


FIG. 10. Idler detection probabilities (top left), signal 1 and signal 2 detection probabilities (top right), signal detector twofold coincidence probabilities and signal detectors with idler in threshold configuration (bottom left), twofold signal and idler in PNR configuration twofold coincidence probabilities. The prediction from the theoretical model is shown for the best-fit parameters in Table I.

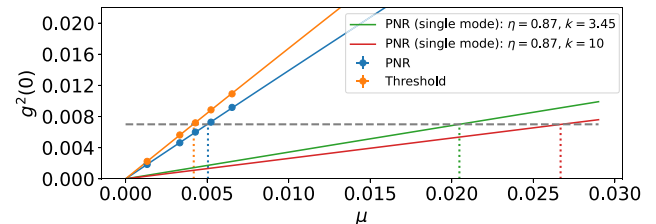


FIG. 11. Correlation function $g^2(0)$ as a function of mean photon number $\mu \ll 1$ for our experiment and improved heralded single-photon sources. The experimental data (large dots) are represented with their uncertainties. The models for the threshold configuration (orange curve) and PNR configuration (blue curve) of our detector are compared with the green and red curves, which correspond to model predictions using improved sources, as discussed in the main text, with key parameters (tree depth k , path efficiencies $\eta \equiv \eta_{s1} = \eta_{s2} = \eta_i$) shown in the inset. Gray dashed line corresponding to a $g^2(0)$ measured in Ref. [28].

C. Improvement with a PNR SNSPD

The reduction of $g^2(0)$ shown in Fig. 9 demonstrates a suppression of multiphoton events. A maximum reduction of 0.118 ± 0.012 at $\mu = 0.327 \pm 0.007$ is observed; it is more clearly indicated in the inset of Fig. 9.

The data and fit for $\mu \ll 1$ is presented in Fig. 11. Configurations (ii) and (i) are denoted by orange and blue colors, respectively, with the data indicated by large dots and the fit by solid curves. To give context, orange and blue dotted lines indicate the μ corresponding to a $g^2(0)$ of 7×10^{-3} (gray dashed line) measured in Ref. [28]. Specifically, we observe a 25% improvement in μ , from 4×10^{-3} (orange dotted line) with configuration (ii), to 5×10^{-3} (blue dotted line) with configuration (i).

To estimate the performance of our experiment with future improvements, we calculate $g^2(0)$ using the properties of our PNR detector ($k = 3.45$, green curve) and those of a PNR detector with a higher tree depth ($k = 10$, red curve). We also assume higher path efficiencies of $\eta_{s1} = \eta_{s2} = \eta_i = 0.87$, which are the product of the coupling (0.91) and detector (0.96) efficiencies from Refs. [46] and [47], respectively, and are among the best achieved to date. With these upgrades, for a $g^2(0)$ of 7×10^{-3} (gray dashed line), we predict an improved $\mu = 20.5 \times 10^{-3}$ (green curve) and $\mu = 26.7 \times 10^{-3}$ (red curve) using our PNR SNSPD and a nearly ideal PNR detector, respectively.

V. DISCUSSION

By measuring the idler mode of a spontaneous parametric down-conversion source using a photon-number-resolving nanowire detector, we reduce the $g^2(0)$ of the signal mode or, on the other hand, increase the probability to generate a photon. The results and key performance metrics of our experiment are supported by a detailed analytical model, which captures multiphoton effects, imperfections, and multiple spectral modes. Using a setup consisting of fiber-coupled and off-the-shelf devices, we generate photons that can be used in quantum information applications, in particular quantum communications [48,49].

To realize an ideal single-photon source [1], a number of improvements to our experiment must be implemented [36]. First, the Schmidt number of our SPDC source must be decreased from its current value of $K \approx 772$ to $K = 1$. This can be accomplished by either narrower spectral filtering of the pairs or increasing the pump pulse bandwidth [50], the use of cavity-enhanced SPDC [51], or by engineering the phase-matching function of the nonlinear crystal [52,53]. A near-unity Schmidt number renders the photons suitable for interference with other independently generated photons in a quantum circuit or network.

Next, the system efficiency should be increased to near unity. Coupling between fibers and devices can be improved with enhanced modal engineering [54] or using

antireflection-coated free-space components [55]. Alternatively, components could be integrated onto the same chip, for instance, using Si- or SiN-on-insulator with SFWM sources [17,56], or using thin-film lithium niobate [57]. Furthermore, multiplexing strategies must be employed to increase the probability of generating a single pair beyond the theoretical maximum of 25% per mode. Such multiplexing, using, for instance, spatial [58,59], temporal [46,60], or frequency modes [61,62], could also be employed to circumvent loss in the signal mode [63]. This requires on-demand feed-forward mode mapping using switches [64], quantum memories [65], or frequency shifters [66], respectively. Feed forward requires the real-time readout that our PNR SNSPD allows. Note that feed forward also allows for temporal filtering of the signal mode, a method that yields a significant reduction in $g^2(0)$ [67–69]. We also point out that our improvement in $g^2(0)$ significantly reduces the number of spatially multiplexed sources (approximately $1/\mu$ for $\mu \ll 1$) that are required to render our heralded photon source to be quasideterministic. For instance, for $g^2(0) = 7 \times 10^{-3}$, in which we observe a 25% improvement in μ from 4×10^{-3} to 5×10^{-3} , see Fig. 11, corresponds to a reduction of the number of multiplexed spatial modes from 250 to 200. Further, with an improved detector efficiency of 0.87 [46,47], only approximately 49 multiplexed modes will be required to quasideterministically generate a heralded single photon.

Multiplexing with feed forward also allows a multimode source to be rendered as a single mode source, i.e., it effectively decreases its Schmidt number to unity [62]. Our broadband SPDC source is naturally suited for frequency multiplexing, as indicated by the strong frequency correlations in our JSI [70]. This suggests our measured $\mu = 5 \times 10^{-3}$ for $g^2(0) = 7 \times 10^{-3}$ exceeds state-of-the-art SPDC sources using threshold detection, as well as quantum dots [28], accounting for such frequency multiplexing.

Additional gains can be offered by improvements to the PNR SNSPD. A higher detector efficiency, i.e., ideally increasing η_d to one, would increase the single-photon discrimination efficiency and improve the fidelity of the heralded single photon. This may be achieved through improvements to the optical stack around the nanowire by replacing the gold mirror with a distributed Bragg reflector mirror [71]. Also, the detector reset time of nearly 100 ns restricts the maximum repetition rate of the source to be approximately 10 MHz. A SNSPD with a reduced reset time based on a lower kinetic inductance nanowire material, or integrated with an active quenching circuit [72], would allow for high single-photon generation rates. A multiplexing method based on multiple PNR SNSPDs would also support a high repetition rate in addition to a substantial increase in detection efficiency [73].

Beyond single-photon sources, extensions of our setup allow efficient generation of qubits or qudits, as well as entanglement swapping using PNR SNSPDs [49]. Further

uses encompass preparation of heralded photon-number states [74] and non-Gaussian continuous-variable states [75], vital resources to realize fault-tolerant photonic quantum computers [76]. Lastly, and of note, by using PNRs to improve teleportation rates [16], alternative applications can benefit including microwave to optical transduction [77]. Recently, we became aware of relevant results achieved independently of this work [78].

ACKNOWLEDGMENTS

We acknowledge partial funding from the Department of Energy BES HEADS-QON Grant No. DE-SC0020376 (on applications related to transduction), QuantiSED SC0019219, and the AQT Intelligent Quantum Networks and Technologies (INQNET) research program. Partial support for this work is provided by the DARPA DSO DETECT, NASA SCaN, and Caltech/JPL PDRDF programs. S.I.D. and A.M. acknowledge partial support from the Brinson Foundation. Part of this research was performed at the Jet Propulsion Laboratory, California Institute of Technology, under contract with NASA. We acknowledge productive discussions with Kayden Taylor, Sergio Escobar, Daniel Oblak, and Cristian Peña. We are grateful to Jason Trevor for technical assistance.

-
- [1] M. D. Eisaman, J. Fan, A. Migdall, and S. V. Polyakov, Invited review article: Single-photon sources and detectors, *Rev. Sci. Instrum.* **82**, 071101 (2011).
- [2] J. L. O'Brien, A. Furusawa, and J. Vučković, Photonic quantum technologies, *Nat. Photonics* **3**, 687 (2009).
- [3] I. Aharonovich, D. Englund, and M. Toth, Solid-state single-photon emitters, *Nat. Photonics* **10**, 631 (2016).
- [4] P. Michler, A. Kiraz, C. Becher, W. Schoenfeld, P. Petroff, L. Zhang, E. Hu, and A. Imamoglu, A quantum dot single-photon turnstile device, *Science* **290**, 2282 (2000).
- [5] A. J. Shields, Semiconductor quantum light sources, *Nat. Photonics* **1**, 215 (2007).
- [6] P. Senellart, G. Solomon, and A. White, High-performance semiconductor quantum-dot single-photon sources, *Nat. Nanotechnol.* **12**, 1026 (2017).
- [7] T. M. Babinec, B. J. Hausmann, M. Khan, Y. Zhang, J. R. Maze, P. R. Hemmer, and M. Lončar, A diamond nanowire single-photon source, *Nat. Nanotechnol.* **5**, 195 (2010).
- [8] H. Barros, A. Stute, T. Northup, C. Russo, P. Schmidt, and R. Blatt, Deterministic single-photon source from a single ion, *New J. Phys.* **11**, 103004 (2009).
- [9] M. Mücke, J. Bochmann, C. Hahn, A. Neuzner, C. Nölleke, A. Reiserer, G. Rempe, and S. Ritter, Generation of single photons from an atom-cavity system, *Phys. Rev. A* **87**, 063805 (2013).
- [10] C. Bradac, W. Gao, J. Forneris, M. E. Trusheim, and I. Aharonovich, Quantum nanophotonics with group IV defects in diamond, *Nat. Commun.* **10**, 5625 (2019).
- [11] S. Bogdanović, M. S. Liddy, S. B. van Dam, L. C. Coenen, T. Fink, M. Lončar, and R. Hanson, Robust nano-fabrication of an integrated platform for spin control in a tunable microcavity, *APL Photonics* **2**, 126101 (2017).
- [12] D. Huber, M. Reindl, Y. Huo, H. Huang, J. S. Wildmann, O. G. Schmidt, A. Rastelli, and R. Trotta, Highly indistinguishable and strongly entangled photons from symmetric GaAs quantum dots, *Nat. Commun.* **8**, 15506 (2017).
- [13] A. Sipahigil, K. D. Jahnke, L. J. Rogers, T. Teraji, J. Isoya, A. S. Zibrov, F. Jelezko, and M. D. Lukin, Indistinguishable Photons from Separated Silicon-Vacancy Centers in Diamond, *Phys. Rev. Lett.* **113**, 113602 (2014).
- [14] H. Bernien, L. Childress, L. Robledo, M. Markham, D. Twitchen, and R. Hanson, Two-Photon Quantum Interference from Separate Nitrogen Vacancy Centers in Diamond, *Phys. Rev. Lett.* **108**, 043604 (2012).
- [15] R. W. Boyd, *Nonlinear Optics* (Academic Press, London, UK, 2020).
- [16] R. Valivarthi, S. I. Davis, C. Peña, S. Xie, N. Lauk, L. Narváez, J. P. Allmaras, A. D. Beyer, Y. Gim, and M. Hussein, *et al.*, Teleportation Systems Toward a Quantum Internet, *PRX Quantum* **1**, 020317 (2020).
- [17] J. Wang, F. Sciarrino, A. Laing, and M. G. Thompson, Integrated photonic quantum technologies, *Nat. Photonics* **14**, 273 (2020).
- [18] J. B. Spring, P. L. Mennea, B. J. Metcalf, P. C. Humphreys, J. C. Gates, H. L. Rogers, C. Söller, B. J. Smith, W. S. Kolthammer, and P. G. Smith, *et al.*, Chip-based array of near-identical, pure, heralded single-photon sources, *Optica* **4**, 90 (2017).
- [19] A. E. Lita, A. J. Miller, and S. W. Nam, Counting near-infrared single-photons with 95% efficiency, *Opt. Express* **16**, 3032 (2008).
- [20] L. A. Jiang, E. A. Dauler, and J. T. Chang, Photon-number-resolving detector with 10 bits of resolution, *Phys. Rev. A* **75**, 062325 (2007).
- [21] M. Fitch, B. Jacobs, T. Pittman, and J. Franson, Photon-number resolution using time-multiplexed single-photon detectors, *Phys. Rev. A* **68**, 043814 (2003).
- [22] M. Colangelo, B. Korzh, J. P. Allmaras, A. D. Beyer, A. S. Mueller, R. M. Briggs, B. Bumble, M. Runyan, M. J. Stevens, and A. N. McCaughan, *et al.*, Impedance-matched differential superconducting nanowire detectors, (2021), preprint [ArXiv:2108.07962](https://arxiv.org/abs/2108.07962).
- [23] C. M. Natarajan, M. G. Tanner, and R. H. Hadfield, Superconducting nanowire single-photon detectors: Physics and applications, *Supercond. Sci. Technol.* **25**, 063001 (2012).
- [24] R. J. Glauber, The quantum theory of optical coherence, *Phys. Rev.* **130**, 2529 (1963).
- [25] M. Takeoka, R.-B. Jin, and M. Sasaki, Full analysis of multi-photon pair effects in spontaneous parametric down conversion based photonic quantum information processing, *New J. Phys.* **17**, 043030 (2015).
- [26] A. Feito, J. Lundeen, H. Coldenstrodt-Ronge, J. Eisert, M. B. Plenio, and I. A. Walmsley, Measuring measurement: Theory and practice, *New J. Phys.* **11**, 093038 (2009).
- [27] D. Achilles, C. Silberhorn, C. Sliwa, K. Banaszek, I. A. Walmsley, M. J. Fitch, B. C. Jacobs, T. B. Pittman, and J. D. Franson, Photon-number-resolving detection using time-multiplexing, *J. Mod. Opt.* **51**, 1499 (2004).

- [28] F. Kaneda and P. G. Kwiat, High-efficiency single-photon generation via large-scale active time multiplexing, *Sci. Adv.* **5**, eaaw8586 (2019).
- [29] F. Marsili, V. B. Verma, J. A. Stern, S. Harrington, A. E. Lita, T. Gerrits, I. Vayshenker, B. Baek, M. D. Shaw, and R. P. Mirin, *et al.*, Detecting single infrared photons with 93% system efficiency, *Nat. Photonics* **7**, 210 (2013).
- [30] D. Zhu, M. Colangelo, B. A. Korzh, Q.-Y. Zhao, S. Frasca, A. E. Dane, A. E. Velasco, A. D. Beyer, J. P. Allmaras, and E. Ramirez, *et al.*, Superconducting nanowire single-photon detector with integrated impedance-matching taper, *Appl. Phys. Lett.* **114**, 042601 (2019).
- [31] D. Zhu, M. Colangelo, C. Chen, B. A. Korzh, F. N. Wong, M. D. Shaw, and K. K. Berggren, Resolving photon numbers using a superconducting nanowire with impedance-matching taper, *Nano Lett.* **20**, 3858 (2020).
- [32] C. Cahall, K. L. Nicolich, N. T. Islam, G. P. Lafyatis, A. J. Miller, D. J. Gauthier, and J. Kim, Multi-photon detection using a conventional superconducting nanowire single-photon detector, *Optica* **4**, 1534 (2017).
- [33] F. Laudenbach, H. Hübel, M. Hentschel, P. Walther, and A. Poppe, Modelling parametric down-conversion yielding spectrally pure photon pairs, *Opt. Express* **24**, 2712 (2016).
- [34] D. E. Zelmon, D. L. Small, and D. Jundt, Infrared corrected sellmeier coefficients for congruently grown lithium niobate and 5 mol.% magnesium oxide-doped lithium niobate, *JOSA B* **14**, 3319 (1997).
- [35] K. Zielnicki, K. Garay-Palmett, D. Cruz-Delgado, H. Cruz-Ramirez, M. F. O'Boyle, B. Fang, V. O. Lorenz, A. B. U'Ren, and P. G. Kwiat, Joint spectral characterization of photon-pair sources, *J. Mod. Opt.* **65**, 1141 (2018).
- [36] A. Christ and C. Silberhorn, Limits on the deterministic creation of pure single-photon states using parametric down-conversion, *Phys. Rev. A* **85**, 023829 (2012).
- [37] M. Zukowski, A. Zeilinger, and H. Weinfurter, Entangling photons radiated by independent pulsed sources, *Ann. N. Y. Acad. Sci.* **755**, 91 (1995).
- [38] D. Klyshko, Use of two-photon light for absolute calibration of photoelectric detectors, *Sov. J. Quantum Electron.* **10**, 1112 (1980).
- [39] F. Bussieres, J. A. Slater, N. Godbout, and W. Tittel, Fast and simple characterization of a photon pair source, *Opt. Express* **16**, 17060 (2008).
- [40] C. Weedbrook, S. Pirandola, R. García-Patrón, N. J. Cerf, T. C. Ralph, J. H. Shapiro, and S. Lloyd, Gaussian quantum information, *Rev. Mod. Phys.* **84**, 621 (2012).
- [41] U. Leonhardt, *Measuring the Quantum State of Light* Vol. 22 (Cambridge University Press, Cambridge, UK, 1997).
- [42] H. Paul, P. Törmä, T. Kiss, and I. Jex, Photon Chopping: New Way to Measure the Quantum State of Light, *Phys. Rev. Lett.* **76**, 2464 (1996).
- [43] E. W. Weisstein, Stirling number of the second kind, From MathWorld—A Wolfram Web Resource. <https://mathworld.wolfram.com/StirlingNumberoftheSecondKind.html>.
- [44] F. James and M. Roos, Minuit: A system for function minimization and analysis of the parameter errors and correlations, *Comput. Phys. Commun.* **10**, 343 (1975).
- [45] H. Dembinski and P. O., *et al.*, scikit-hep/iminuit (2020).
- [46] F. Kaneda, K. Garay-Palmett, A. B. U'Ren, and P. G. Kwiat, Heralded single-photon source utilizing highly non-degenerate, spectrally factorable spontaneous parametric downconversion, *Opt. Express* **24**, 10733 (2016).
- [47] M. K. Akhlaghi, E. Schelew, and J. F. Young, Waveguide integrated superconducting single-photon detectors implemented as near-perfect absorbers of coherent radiation, *Nat. Commun.* **6**, 8233 (2015).
- [48] C. Bennett and G. Brassard, in *Conf. on Computers, Systems and Signal Processing*, Vol. 175 (1984).
- [49] H. Krovi, S. Guha, Z. Dutton, J. A. Slater, C. Simon, and W. Tittel, Practical quantum repeaters with parametric down-conversion sources, *Appl. Phys. B* **122**, 52 (2016).
- [50] J. Rarity, Interference of single photons from separate sources, *Ann. N. Y. Acad. Sci.* **755**, 624 (1995).
- [51] T. Herzog, J. Rarity, H. Weinfurter, and A. Zeilinger, Frustrated Two-Photon Creation via Interference, *Phys. Rev. Lett.* **72**, 629 (1994).
- [52] P. J. Mosley, J. S. Lundeen, B. J. Smith, P. Wasylczyk, A. B. U'Ren, C. Silberhorn, and I. A. Walmsley, Heralded Generation of Ultrafast Single Photons in Pure Quantum States, *Phys. Rev. Lett.* **100**, 133601 (2008).
- [53] C. J. Xin, J. Mishra, C. Chen, D. Zhu, A. Shams-Ansari, C. Langrock, N. Sinclair, F. N. C. Wong, M. M. Fejer, and M. Lončar, Spectrally separable photon-pair generation in dispersion engineered thin-film lithium niobate, *Opt. Lett.* **47**, 2830 (2022).
- [54] B. S. Kawasaki, K. O. Hill, and R. Lamont, Biconical-taper single-mode fiber coupler, *Opt. Lett.* **6**, 327 (1981).
- [55] L. K. Shalm, E. Meyer-Scott, B. G. Christensen, P. Bierhorst, M. A. Wayne, M. J. Stevens, T. Gerrits, S. Glancy, D. R. Hamel, and M. S. Allman, *et al.*, Strong Loophole-Free Test of Local Realism, *Phys. Rev. Lett.* **115**, 250402 (2015).
- [56] J. W. Silverstone, D. Bonneau, K. Ohira, N. Suzuki, H. Yoshida, N. Iizuka, M. Ezaki, C. M. Natarajan, M. G. Tanner, and R. H. Hadfield, *et al.*, On-chip quantum interference between silicon photon-pair sources, *Nat. Photonics* **8**, 104 (2014).
- [57] D. Zhu, L. Shao, M. Yu, R. Cheng, B. Desiatov, C. Xin, Y. Hu, J. Holzgrafe, S. Ghosh, and A. Shams-Ansari, *et al.*, Integrated photonics on thin-film lithium niobate, *Adv. Opt. Photonics* **13**, 242 (2021).
- [58] M. J. Collins, C. Xiong, I. H. Rey, T. D. Vo, J. He, S. Shahnia, C. Reardon, T. F. Krauss, M. J. Steel, A. S. Clark, and B. J. Eggleton, Integrated spatial multiplexing of heralded single-photon sources, *Nat. Commun.* **4**, 2582 (2013).
- [59] G. J. Mendoza, R. Santagati, J. Munns, E. Hemsley, M. Piekarz, E. Martín-López, G. D. Marshall, D. Bonneau, M. G. Thompson, and J. L. O'Brien, Active temporal and spatial multiplexing of photons, *Optica* **3**, 127 (2016).
- [60] C. Xiong, X. Zhang, Z. Liu, M. J. Collins, A. Mahendra, L. G. Helt, M. J. Steel, D.-Y. Choi, C. J. Chae, P. H. W. Leong, and B. J. Eggleton, Active temporal multiplexing of indistinguishable heralded single photons, *Nat. Commun.* **7**, 10853 (2016).
- [61] C. Joshi, A. Farsi, S. Clemmen, S. Ramelow, and A. L. Gaeta, Frequency multiplexing for quasi-deterministic heralded single-photon sources, *Nat. Commun.* **9**, 847 (2018).

- [62] M. G. Puigibert, G. Aguilar, Q. Zhou, F. Marsili, M. Shaw, V. Verma, S. Nam, D. Oblak, and W. Tittel, Heralded Single Photons Based on Spectral Multiplexing and Feed-Forward Control, *Phys. Rev. Lett.* **119**, 083601 (2017).
- [63] N. Sinclair, E. Saglamyurek, H. Mallahzadeh, J. A. Slater, M. George, R. Ricken, M. P. Hedges, D. Oblak, C. Simon, and W. Sohler, *et al.*, Spectral Multiplexing for Scalable Quantum Photonics using an Atomic Frequency Comb Quantum Memory and Feed-Forward Control, *Phys. Rev. Lett.* **113**, 053603 (2014).
- [64] P. Xu, J. Zheng, J. K. Doylend, and A. Majumdar, Low-loss and broadband nonvolatile phase-change directional coupler switches, *ACS Photonics* **6**, 553 (2019).
- [65] A. I. Lvovsky, B. C. Sanders, and W. Tittel, Optical quantum memory, *Nat. Photonics* **3**, 706 (2009).
- [66] Y. Hu, M. Yu, D. Zhu, N. Sinclair, A. Shams-Ansari, L. Shao, J. Holzgrafe, E. Puma, M. Zhang, and M. Lončar, On-chip electro-optic frequency shifters and beam splitters, *Nature* **599**, 587 (2021).
- [67] G. Brida, I. P. Degiovanni, M. Genovese, F. Piacentini, P. Traina, A. Della Frera, A. Tosi, A. Bahgat Shehata, C. Scarcella, and A. Gulinatti, *et al.*, An extremely low-noise heralded single-photon source: A breakthrough for quantum technologies, *Appl. Phys. Lett.* **101**, 221112 (2012).
- [68] S. Krapick, H. Herrmann, V. Quiring, B. Brecht, H. Suche, and C. Silberhorn, An efficient integrated two-color source for heralded single photons, *New J. Phys.* **15**, 033010 (2013).
- [69] M. Massaro, E. Meyer-Scott, N. Montaut, H. Herrmann, and C. Silberhorn, Improving spdc single-photon sources via extended heralding and feed-forward control, *New J. Phys.* **21**, 053038 (2019).
- [70] T. Hiemstra, T. Parker, P. Humphreys, J. Tiedau, M. Beck, M. Karpiński, B. Smith, A. Eckstein, W. Kolthammer, and I. Walmsley, Pure Single Photons from Scalable Frequency Multiplexing, *Phys. Rev. Appl.* **14**, 014052 (2020).
- [71] D. V. Reddy, R. R. Nerem, S. W. Nam, R. P. Mirin, and V. B. Verma, Superconducting nanowire single-photon detectors with 98% system detection efficiency at 1550 nm, *Optica* **7**, 1649 (2020).
- [72] P. Ravindran, R. Cheng, H. Tang, and J. C. Bardin, Active quenching of superconducting nanowire single photon detectors, *Opt. Express* **28**, 4099 (2020).
- [73] F. Bodog, M. Mechler, M. Koniorczyk, and P. Adam, Optimization of multiplexed single-photon sources operated with photon-number-resolving detectors, *Phys. Rev. A* **102**, 013513 (2020).
- [74] M. Cooper, L. J. Wright, C. Söller, and B. J. Smith, Experimental generation of multi-photon Fock states, *Opt. Express* **21**, 5309 (2013).
- [75] D. Su, C. R. Myers, and K. K. Sabapathy, Conversion of Gaussian states to non-Gaussian states using photon-number-resolving detectors, *Phys. Rev. A* **100**, 052301 (2019).
- [76] J. E. Bourassa, R. N. Alexander, M. Vasmer, A. Patil, I. Tzitrin, T. Matsuura, D. Su, B. Q. Baragiola, S. Guha, and G. Dauphinais, *et al.*, Blueprint for a scalable photonic fault-tolerant quantum computer, *Quantum* **5**, 392 (2021).
- [77] C. Zhong, Z. Wang, C. Zou, M. Zhang, X. Han, W. Fu, M. Xu, S. Shankar, M. H. Devoret, H. X. Tang, and L. Jiang, Proposal for Heralded Generation and Detection of Entangled Microwave–Optical-Photon Pairs, *Phys. Rev. Lett.* **124**, 010511 (2020).
- [78] S. Sempere-Llagostera, G. S. Thekkadath, R. B. Patel, W. S. Kolthammer, and I. A. Walmsley, Reducing $g(2)(0)$ of a parametric down-conversion source via photon-number resolution with superconducting nanowire detectors, *Opt. Express* **30**, 3138 (2022).

Correction: A proof correction regarding a term in Eq. (10) was implemented incorrectly and has been set right.